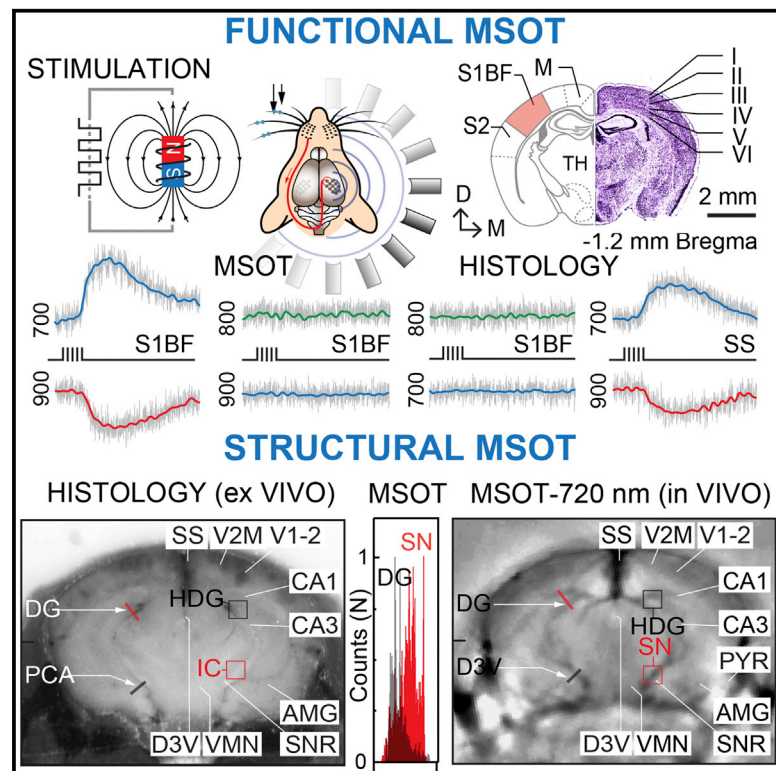


Cell Reports

Spatial and Spectral Mapping and Decomposition of Neural Dynamics and Organization of the Mouse Brain with Multispectral Optoacoustic Tomography

Graphical Abstract



Authors

Ivan Olefir, Ara Ghazaryan, Hong Yang, ..., George Sergiadis, Vasilis Ntziachristos, Saak V. Ovsepian

Correspondence

v.ntziachristos@helmholtz-muenchen.de (V.N.),
saak.ovsepian@gmail.com (S.V.O.)

In Brief

Olefir et al. apply multispectral optoacoustic (photoacoustic) tomography (MSOT) for noninvasive spatial and spectral mapping and decomposition of neural dynamics and organization of the intact mouse brain *in vivo*. The results extend the boundaries of noninvasive high-resolution observations beyond the reach of intravital optical neuroimaging in small-animal studies.

Highlights

- Noninvasive functional and structural neuroimaging in mice using MSOT
- Resting and activity-dependent response mapped on entire brain cross-sections
- Connectivity between various structures revealed with coherence analysis
- High-resolution structural tomography achieved based on endogenous contrasts



Spatial and Spectral Mapping and Decomposition of Neural Dynamics and Organization of the Mouse Brain with Multispectral Optoacoustic Tomography

Ivan Olefir,^{1,2} Ara Ghazaryan,¹ Hong Yang,¹ Jaber Malekzadeh-Najafabadi,¹ Sarah Glasl,¹ Panagiotis Symvoulidis,^{1,2} Valerie B. O'Leary,³ George Sergiadis,⁴ Vasilis Ntziachristos,^{1,2,7,8,*} and Saak V. Ovsepian^{1,2,5,6,7,*}

¹Institute of Biological and Medical Imaging (IBMI), Helmholtz Zentrum Munich, Ingolstadter Landstrasse 1, 85764 Neuherberg, Germany

²Chair of Biological Imaging, Technical University Munich, 81675 Munich, Germany

³Department of Medical Genetics, Third Faculty of Medicine of Charles University, 11636 Prague, Czech Republic

⁴Department of Electrical and Computer Engineering, Aristotle University, 54124 Thessaloniki, Greece

⁵Department of Experimental Neurobiology, National Institute of Mental Health, Topolová 748, 25067 Klecany, Czech Republic

⁶Department of Psychiatry and Medical Psychology, Third Faculty of Medicine of Charles University, 11636 Prague, Czech Republic

⁷These authors contributed equally

⁸Lead Contact

*Correspondence: v.ntziachristos@helmholtz-muenchen.de (V.N.), saak.ovsepian@gmail.com (S.V.O.)

<https://doi.org/10.1016/j.celrep.2019.02.020>

SUMMARY

In traditional optical imaging, limited light penetration constrains high-resolution interrogation to tissue surfaces. Optoacoustic imaging combines the superb contrast of optical imaging with deep penetration of ultrasound, enabling a range of new applications. We used multispectral optoacoustic tomography (MSOT) for functional and structural neuroimaging in mice at resolution, depth, and specificity unattainable by other neuroimaging modalities. Based on multispectral readouts, we computed hemoglobin gradient and oxygen saturation changes related to processing of somatosensory signals in different structures along the entire subcortical-cortical axis. Using temporal correlation analysis and seed-based maps, we reveal the connectivity between cortical, thalamic, and sub-thalamic formations. With the same modality, high-resolution structural tomography of intact mouse brain was achieved based on endogenous contrasts, demonstrating near-perfect matches with anatomical features revealed by histology. These results extend the limits of noninvasive observations beyond the reach of standard high-resolution neuroimaging, verifying the suitability of MSOT for small-animal studies.

INTRODUCTION

Unveiling a structure-functional relationship in the nervous system is one of the key priorities of neuroimaging. In this pursuit, optical imaging has been the main workhorse, enabling over many decades the high-resolution structural brain imaging (Witt et al., 2009). With superb contrast, resolution, and multiplexing capabilities, optical interrogation has also recently become an

integral part of functional neuroimaging, empowering sensing of voltage and calcium dynamics of individual neurons and synaptic connections (Chen et al., 2011; Grienberger et al., 2014; Perron et al., 2009; Peterka et al., 2011; Stettler et al., 2006). Notwithstanding these advances, investigation of the brain using light has several fundamental limitations, due to diffraction and scattering, which constrain observations to the surface (Hillman, 2007; Hong et al., 2014; Ntziachristos, 2010). For microscopy, penetration of several hundred microns into brain has been achieved using two-photon excitation via cranial opening, which could be extended further by surgical removal of superficial tissue mass, with downsides of invasiveness and loss of circuit integrity (Dombeck et al., 2010; Helmchen and Denk, 2005; Kerr and Denk, 2008; Willem et al., 2015). Using three-photon GCaMP6 excitation, the activity of neurons in the dorsal hippocampus was recently recorded *in vivo*, albeit with major depth-dependent loss of spatial resolution (Ouzounov et al., 2017). For macroscopic brain imaging usage, the limits set by light scattering have been partly surmounted by the utilization of diffusive imaging methods such as diffuse optical tomography (DOT) and near-infrared spectroscopy (NIRS), which enabled measurements in thick samples, but with poor spatial resolution (Boas et al., 2004; Culver et al., 2003; Eggebrecht et al., 2014; Siegel et al., 1999).

Unlike optical imaging, high-resolution radiological methods such as fMRI and ultrasonography (US) enable excellent penetration with 3D isotropic visualization of intact biological samples. However, the principal downfall of fMRI is its low sensitivity, which limits spatial and especially temporal resolution (Denic et al., 2011; Hoyer et al., 2014; Jonckers et al., 2015; Logothetis, 2008), above all detrimental in small-animal studies, where miniature brain size and tiny structures downgrade the data quality (Farahani et al., 1990; Hoyer et al., 2014; Yang et al., 2006). Unlike fMRI, functional US (fUS) affords first-rate resolution in time and space, empowering exquisite connectivity analysis and hemodynamic readouts in murine and human applications (Errico et al., 2015; Gesnik et al., 2017; Macé et al., 2011; Osmanski et al., 2014). While suitable for mapping brain activation by sensory



inputs, high-resolution fUS in adult murine models requires skull thinning or cranial opening (Macé et al., 2011; Osmanski et al., 2014). Using optimized US sequence with specialized probes, a recent report showed the feasibility of noninvasive transcranial fUS in young mice (< 1 month old [m.o.]), validating its utility for neuroimaging in behavioral studies (Tiran et al., 2017).

Optoacoustic (photoacoustic) imaging combines the superb contrast mechanisms of optical imaging with the high resolution and penetration depth of US (Beard, 2011; Ntziachristos et al., 2005; Taruttis and Ntziachristos, 2015). Despite unique capacities for multiscale and multispectral interrogation of thick biological samples, optoacoustic functional neuroimaging so far has remained largely confined to the cerebral cortex (Liao et al., 2012; Nasirivanaki et al., 2014; Tang et al., 2015; Wang et al., 2003, 2013; Yao et al., 2015). The majority of functional neuroimaging reports have also neglected the multispectral assets of the methodology, using only a single illumination wavelength (Liao et al., 2012; Nasirivanaki et al., 2014; Ovsepian et al., 2017; Wang et al., 2003; Yao and Wang, 2014). A few attempts at mapping functional dynamics of brain circuits and hemoglobin gradient changes in deeper brain compartments have been limited to studies of drug-induced seizure or solid tumor xenografts, with dubious physiological relevance (Burton et al., 2013; Gottschalk et al., 2017). Finally, reports using optoacoustic imaging for structural brain studies *in vivo* have succumbed to visualization of large superficial vessels and major anatomical references (Laufer et al., 2009; Lin et al., 2015; Razansky et al., 2011; Stein et al., 2009).

Thus, to date, the most valuable assets of optoacoustic interrogation neither have been properly validated nor utilized for brain imaging (Ovsepian et al., 2017). In this study, we set out to address some of the omission by testing the efficacy of multispectral optoacoustic tomography (MSOT) for high-resolution label-free functional and structural imaging with reconstruction of the entire mouse brain. We visualize, map, and decompose the spatial and spectral characteristics of a neurovascular response induced by whisker inputs on the entire forebrain cross-sections within intact mice. Based on the temporal coherence of hemodynamic signals and oxygen saturation gradients, we reconstruct the connectivity involved in processing and integration of somatosensory signals along the entire subcortical-cortical axis, which replicates closely the circuitry revealed by neurophysiological studies and tract tracing. Finally, we make original use of MSOT for label-free and contrast-based imaging of mouse brain anatomy and tract tracing *ex vivo* and *in vivo*, to relate volumetric data with results of light-microscopic observations.

RESULTS

Despite outstanding capabilities for high-resolution interrogation and volumetric imaging of deep tissue, the vast majority of functional optoacoustic brain studies in small-animal models have so far been confined to the cortex. To date, activity-related changes in hemodynamic gradients within deep compartments of the brain have been unexplored. Taking advantage of the strong central representation and well-defined connections of somatosensory whisker projections of mice, we imaged the neurovascular responses related to activity and processing of whisker

inputs on the entire forebrain cross-sections using MSOT (Figures S1–S3). We applied whisker stimulation (mechanical deflections) and monitored changes in deoxyhemoglobin (Hb) and oxyhemoglobin (HbO₂) gradients in the brain, with computed tissue oxygenation (sO₂) level.

Figures 1A–1C show the experimental layout of functional MSOT studies and illustrates a mouse brain cross-section containing the somatosensory barrel cortex along with several major anatomical structures, together with traces of Hb, HbO₂, and isosbestic point (700, 900, and 800 nm) signal changes as well as traces from negative control experiments collected from mice without whiskers stimulation. While in all experimental trials initial changes in Hb gradients and sO₂ signals related to the activation of whisker inputs were most prominent in the somatosensory barrel field of the contralateral side, over a short period of time, the evoked responses spread over the adjacent somatosensory cortex hindlimb and primary motor areas, as well as ipsilateral somatosensory barrel and motor fields. Interestingly, under our experimental settings, the total blood volume (i.e., signal detected at 800 nm) in activated cortical regions remained largely unchanged, possibly due to weak intensity of whisker inputs. Figures 1D–1G illustrate a representative series of MSOT images overlaid with thresholded Hb, HbO₂, and sO₂ maps at consecutive time points from two experiments. Analysis of signal density changes across different layers of the somatosensory barrel field revealed a distinctly lamellar pattern of the hemodynamic response with significant differences evident in the signal onset and distribution across different cortical layers (Figure 1H). Unlike HbO₂ changes concomitantly across multiple layers of the barrel cortex and reaching the highest intensity in the superficial compartments, the Hb response first appeared in L4–L5 and spread toward both the superficial and deeper cortical layers. Importantly, all alterations in hemodynamic signals related to the somatosensory whisker inputs were stimulus specific, as similar trials with non-magnetized whiskers showed no HbO₂ or Hb changes (Figure 1C). Likewise, in similar experiments with two consecutive series of whisker stimulation, a strong activity-dependent depression in the response to the second stimulation series was observed, in line with history-dependent plasticity of the hemodynamic response (Figure S4).

As somatosensory inputs to the barrel cortex are conveyed through the lemniscal route, via ventral and posterior thalamic relay nuclei, and through extrathalamic modulatory tracts, via basal forebrain projections (Brecht et al., 2004; Zaborszky et al., 2015), we set out to investigate whether neurovascular response changes related to whisker inputs can be detected in these and other functionally associated deep-brain structures. Figures 2A–2C show three consecutive MSOT cross-sections of a mouse brain with a series of Hb and HbO₂ recordings related to the activation of whisker inputs. As can be readily seen, the amplitude of hemodynamic response strongly depends on the anatomical plane, with the strongest changes in Hb gradients confined to the cross-section containing the somatosensory barrel field and associated thalamic nuclei of the contralateral side. Extending the analysis of stimulation-evoked responses with sO₂ measurements over extensive brain areas revealed activation of wider fields, involving ventral and reticular thalamic nuclei, basal forebrain, and amygdala, with however

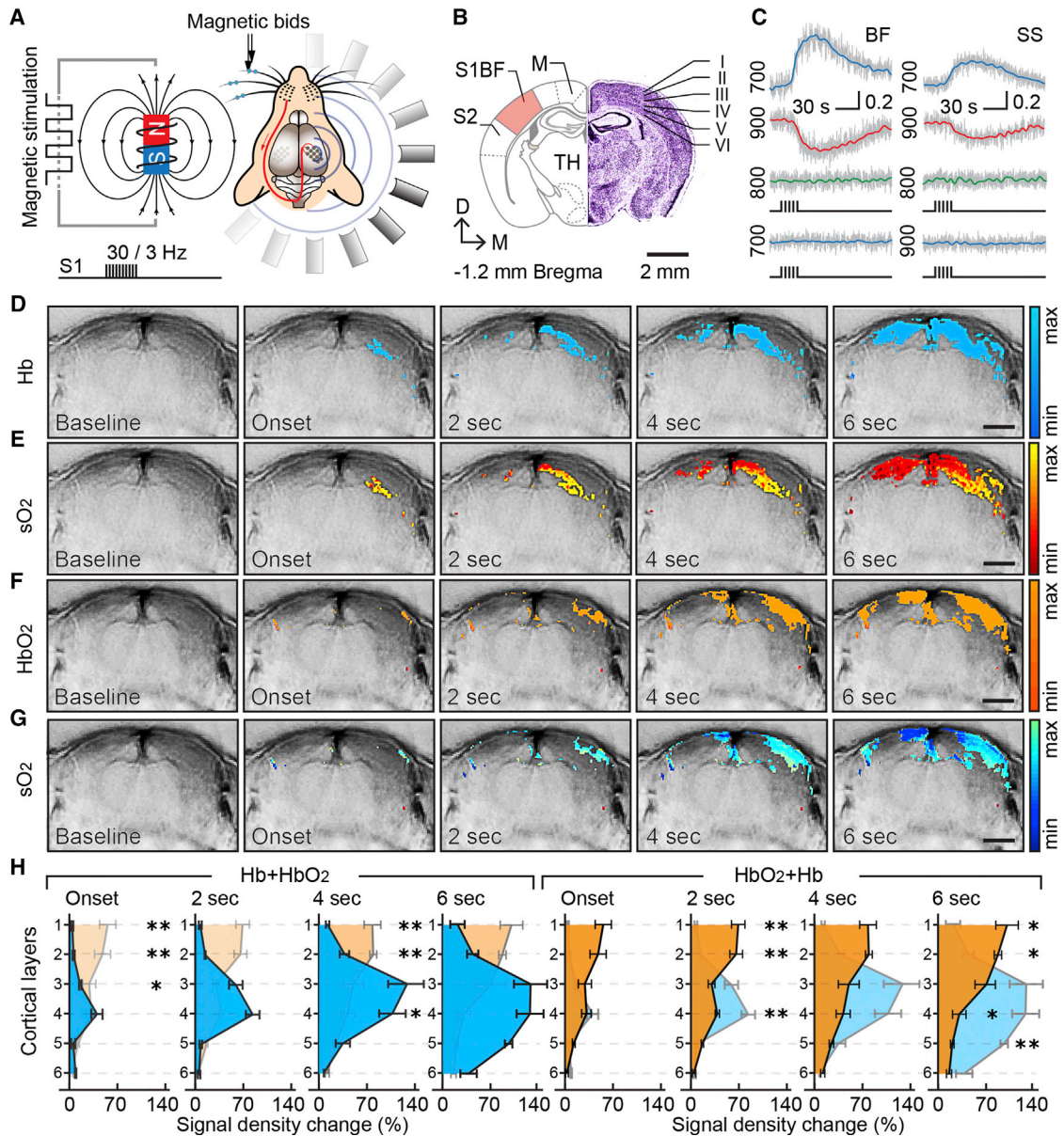


Figure 1. Functional MSOT of Whisker-Induced Response in the Somatosensory Barrel Cortex

(A) Schematic of the experimental design of whisker stimulation with pull-push magnet and brain imaging with MSOT.
 (B) Representation of mouse brain cross-section containing anatomical references such as somatosensory barrel cortex (S1BF), S2 somatosensory field (S2), and motor cortex (M) (left), with Nissl-stained brain slice of corresponding plane showing cortical layers of the S1BF (right).
 (C) Typical traces of HbO₂ (900 nm), Hb (700 nm), and isosbestic (800 nm) signal from experimental group (top), and HbO₂ and Hb signals from negative control group verifying that changes in Hb and HbO₂ signals are specific to activation of whisker inputs.
 (D–G) Consecutive time series of anatomical brain images overlaid with Hb (D), HbO₂ (F), and sO₂ (E and G) maps before (baseline) and after (2-s increments) whisker stimulation. Activation maps presented in different colors show pixel-wise changes in the intensity of MSOT signal related to the stimulation of whisker inputs, with signal intensity changes presented in arbitrary units.
 (H) Distribution and dynamics of the whisker evoked Hb, HbO₂, and sO₂ signal density across different layers of S1BF of the somatosensory cortex. Graphs present means and SEM of signal density changes in different cortical layers from six independent trials with their comparison (*p < 0.05; **p < 0.005; unpaired t test).

no consistent response detectable in areas corresponding to lateral ventricles (Figures 2D–2G).

Next, the extent of the temporal coherence in the neurovascular response between multiple brain regions was analyzed, with

results summarized in cross-correlation matrices of Hb, HbO₂, and sO₂ signals collected across entire brain cross-sections containing the somatosensory barrel field and related structures (Figures 3A–3D). Analogous measurements from negative

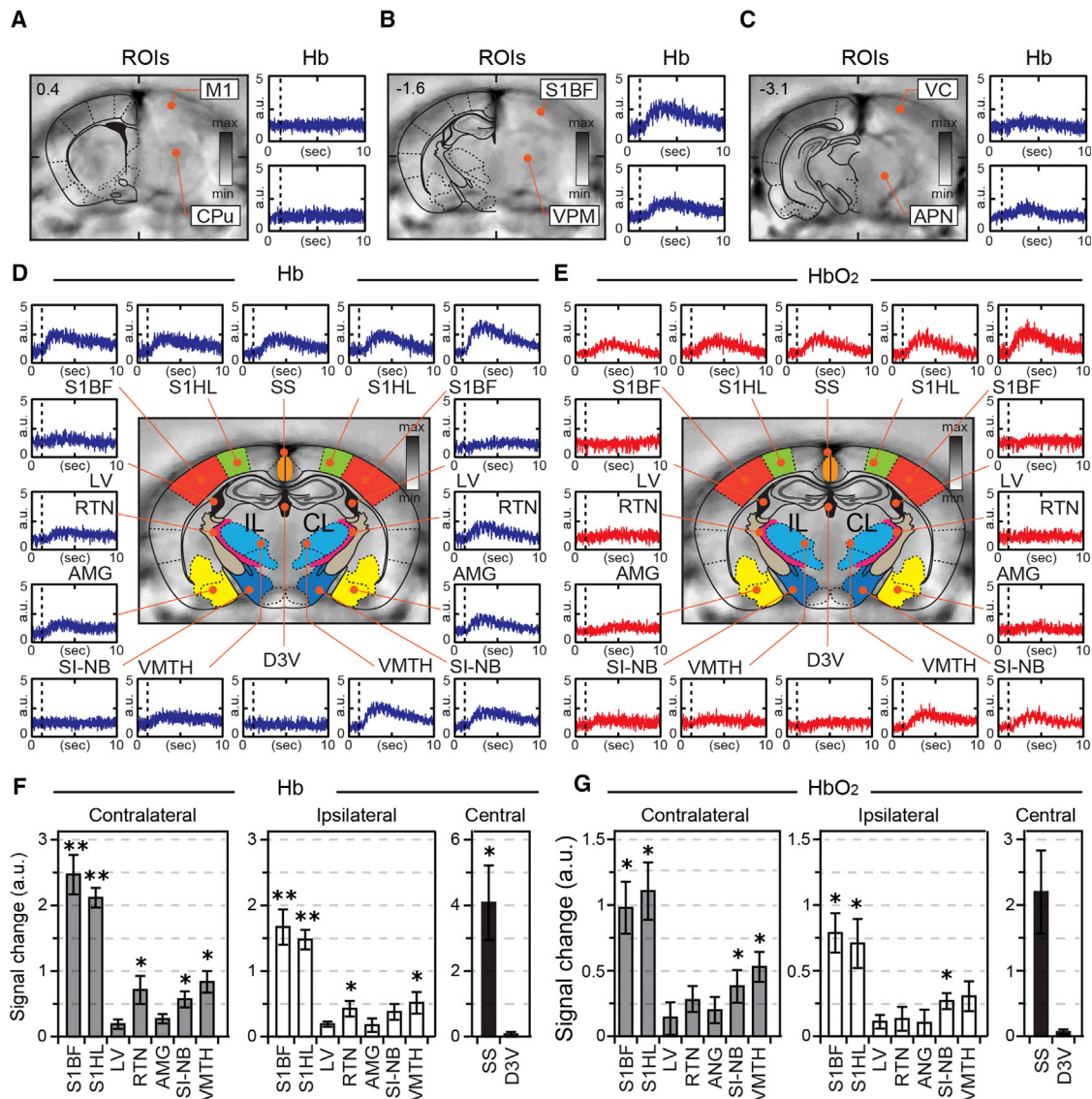


Figure 2. Location Specificity of Hemodynamic Changes across Mouse Brains Induced by Whisker Inputs

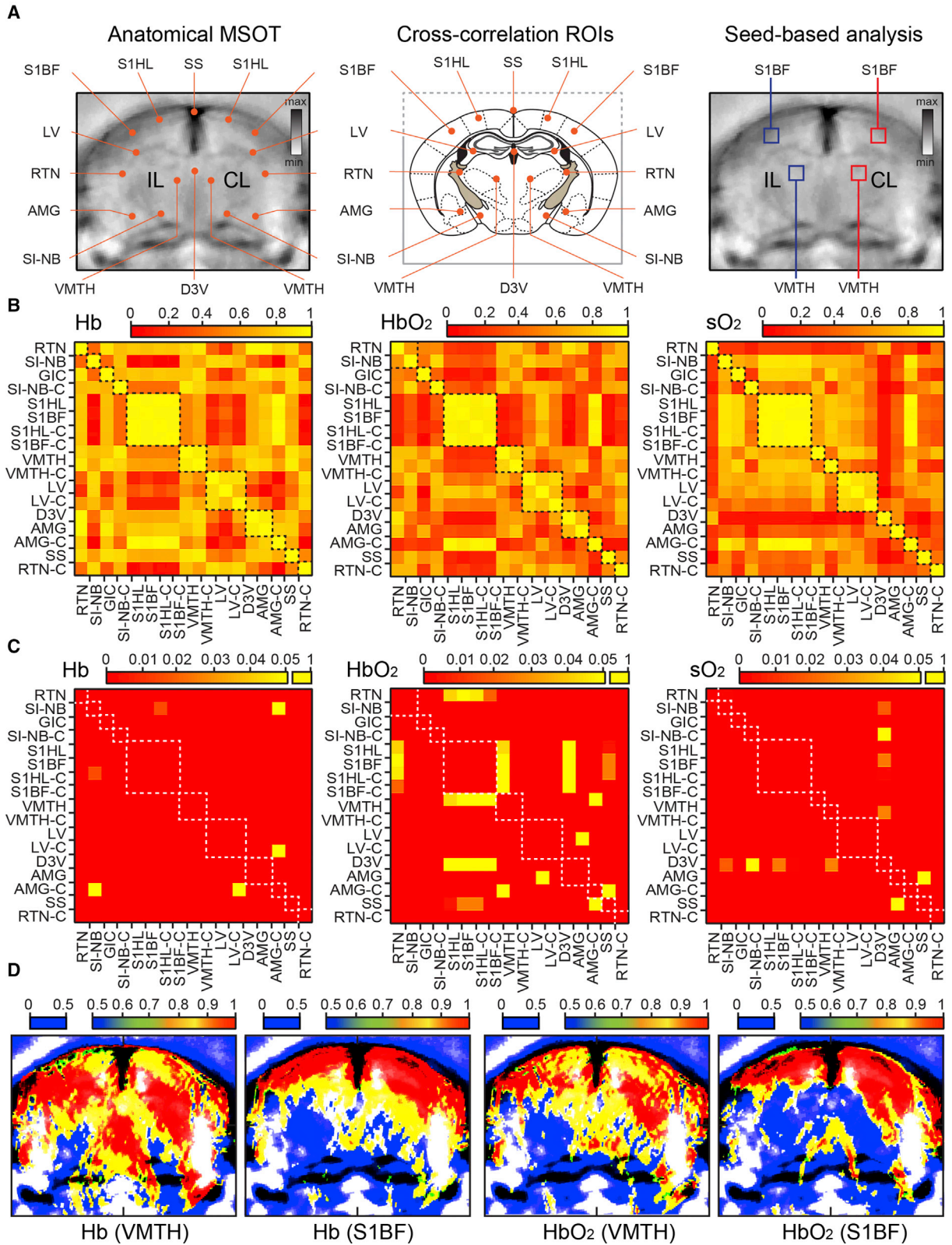
(A–C) Consecutive anatomical MSOT images of mouse brain overlaid with schematic maps of corresponding planes (A, B, and C; left part) with representative recordings of Hb signal from marked regions of interest (ROIs) (A, B, and C; right). Anatomical references: M1, motor cortex; CPU, caudate putamen; S1BF, somatosensory cortex barrel field; VPM, ventral posterior nucleus; VC, visual cortex; APN, anterior pretectal nucleus. Note that Hb changes are specific to the anatomical plane containing S1BF.

(D and E) Typical recordings of Hb (D) and HbO₂ (E) signal from selected ROIs of the mouse brain. IL and CL, ipsilateral and contralateral to the stimulation side. RTN, reticular thalamic nucleus; SI-NB, substantia innominata nucleus basal; S1HL, primary somatosensory, hindlimb; S1BF, primary somatosensory, barrel field; VMTH, ventromedial thalamic nucleus; LV, lateral ventricle; D3V, third dorsal ventricle; AMG, amygdala; SS, sagittal sinus; AMG, amygdala. For illustration purposes, all functional readouts have been inverted to represent more clearly the relative change.

(F and G) Summary graphs illustrating the mean values with SEM of Hb (F) and HbO₂ (G) signal changes (i.e., peak amplitude) in different brain compartments pulled from six independent trials with their comparison (*p < 0.05; **p < 0.005; unpaired t test).

control experiments, without activation of whisker inputs, are shown in [Figures S5A and S5B](#). As can be readily appreciated, repetitive whisker stimulation activates rapid and temporally coherent hemodynamic response in the somatosensory barrel fields as well as in adjacent somatosensory hindlimb areas of both sides. In addition, coherent activation of a hemodynamic response was detectable in related reticular and ventral thalamic

nuclei, as well as throughout the basal forebrain area, which correlated with the response of the barrel field in a statistically significant fashion ([Figure 3C](#)). Of note, the extent of functional coupling of evoked activity and correlation indexes were consistently higher in Hb and sO₂ graphs compared to HbO₂. Alterations in the hemodynamic signal induced by the activation of the somatosensory inputs were also readily detectable on the



(legend on next page)

correlation seed maps of the entire brain cross-sections, when the contralateral ventromedial thalamic nucleus or the somatosensory barrel field were taken as the seed for such analysis (Figure 3D). Consistent with the results of cross-correlation maps, stimulation-related hemodynamic changes synchronized with the seed areas were detectable in reticular and ventral thalamic nuclei, as well as in the basal forebrain area.

Having verified the *in vivo* functional neuroimaging capacities of MSOT across the entire cross-section of the mouse brain, we set to explore and characterize its capabilities as a high-resolution anatomical imaging tool, to verify the accurate assignment of functional readouts to various brain structures. Serial cross-sectional anatomical images of the mouse brain were acquired along the rostro-caudal axis at 0.1 mm steps *in vivo* followed by *ex vivo* imaging without perfusion or after perfusion. Figures 4A–4E present consecutive coronal and horizontal anatomical scans of an *ex vivo* mouse brain at 740-nm wavelength and relate them with anatomical references from the mouse brain atlas. As is clearly visible, at the specified wavelength as well as throughout almost the entire range of the NIR window (700–900 nm), the endogenous absorbers of perfused (bloodless) brains strongly contribute to the formation of anatomical MSOT images (Figures 4C–4E and S6). Indeed, the distinctly stratified and compartmented appearance of brains in coronal cross-sections with a lamellar outlook of olfactory bulbs, along with numerous structural details within the inner forebrain, midbrain, and hindbrain, including cerebellum and brainstem, recapitulate with high fidelity the schematized features of the corresponding anatomical planes from the brain atlas (Figures 4A–4E; Videos S4 and S5). To verify more rigorously the relationship of the structural features as revealed by *ex vivo* MSOT with major anatomical formations of the mouse brain, we compared coronal MSOT scans with structural details on matching stereotactic matching cross-sections enhanced with Nissl staining, captured at low magnification light microscopy (Figures 5A and 5B). As can be readily seen, there is a near-perfect correspondence between the coarse and fine features of the two series of images, with structures revealed by histology also clearly visible and quantifiable on MSOT cross-sections. Importantly, spectral decomposition of images revealed highly localized and specific traits across various brain regions, with melanin-rich midbrain dopaminergic nuclei as well as myelinated bundles of the midbrain, hypothalamus, and medulla readily discernable. In the ventral midbrain and dorsal medulla, for instance, neuro-melanin-rich substantia nigra pars compacta (SNc) and adrenergic pontine-reticular nuclei can be readily delineated on the MSOT scans (Figures 5C–5F).

Because hemoglobin is the principal endogenous chromophore and the main source of optoacoustic signal *in vivo*, its fairly

uniform presence throughout the brain degrades structural features formed by other endogenous absorbers. To more rigorously define the anatomical brain imaging capabilities of MSOT *in vivo*, we compared the major structural features exposed by MSOT in the living animal with those captured with camera on the cryosliced frozen mouse head. As illustrated on a series of images (Figure 6A; Video S6), numerous major anatomical features visible on coronal cryosections were also readily discernable on MSOT cross-sections acquired at 720 nm, showing a near-perfect cross-correspondence. Similar to the *ex vivo* MSOT brain images, the structures revealed by anatomical MSOT *in vivo* could be quantified using morphometric tools and methods (Figures 6B and 6C), although the contrast and prominence of superficial and deep structural details are more distinguishable in *ex vivo* images. To find out whether the deep neuroimaging imaging capabilities of MSOT *in vivo* can be further enhanced using exogenous contrast agents, we applied Di-R for visualizing the ventricular system of the mouse brain and for tracing nigrostriatal dopaminergic projections. The high extinction coefficient of Di-R in aqueous medium makes it ideal for imaging the ventricular system as well as tracing water-rich axonal bundles. Two days after tracer injection in the dorsal chamber of the lateral ventricle, or in the caudate nucleus, *in vivo* MSOT scans of the entire brain were acquired, followed by perfusion of mice and histological verification of injection sites and visualization of the labeling of neuronal tracts, using light microscopy (Figures 7A–7J). In mice injected with Di-R in the dorsal cistern of the lateral ventricle, 3D reconstruction and spectral unmixing showed strong labeling of the ventricular system of the injected side, with dorsal, lateral, and ventral chambers readily visible (Figures 7A–7C). These anatomical features revealed with MSOT were further verified by low-power fluorescence imaging of corresponding brain cross-sections (Figures 7D and 7E). Similarly, in mice receiving Di-R injection in the dorsal striatum, the site of tracer infusion could be visualized on *in vivo* MSOT cross-sections, as also confirmed by *ex vivo* cryo-slicing and histology (Figures 7F–7H). We could not, however, visualize the nigro-striatal dopaminergic projections or SNc nucleus on whole-brain MSOT scans, even though the presence of Di-R dopaminergic axons and neurons were detectable with immunostaining and light microscopy (Figures 7I and 7J).

DISCUSSION

High-resolution imaging of large-scale neural dynamics and the organization of the brain in intact animal models are of major relevance to basic and translational neuroscience, relating specific functional processes to various structures without disruption of tissue homeostasis and integrity. Despite the major

Figure 3. Temporal Coherence of Hemodynamic Changes Induced by Stimulation of Whisker Inputs in Mouse Brain

(A) Structural MSOT images (left and right panels) with marked ROIs used in cross-correlation analysis (left) and in seed-based correlation mapping the functional connectome (right), along with schematized map of corresponding brain plane with anatomical references (middle). For abbreviations, see Figure 2 legend.

(B and C) Correlation matrix of Hb, HbO₂, and sO₂ illustrating the degree of temporal coherence of hemodynamic response induced by whisker inputs (B) and corresponding graph of the distribution of p values of same ROIs (C).

(D) Seed-based correlation maps of the same brain illustrating areas with temporally coherent changes in Hb and HbO₂ signals (i.e., co-activation) in response to whisker inputs. Whisker input driven changes of the hemodynamic signals in the contralateral somatosensory cortex barrel field (S1BF) and contralateral ventromedial thalamic nucleus (VMTH) have been used as seeds for current coherence maps, with the degree of correlation presented in the color bars.

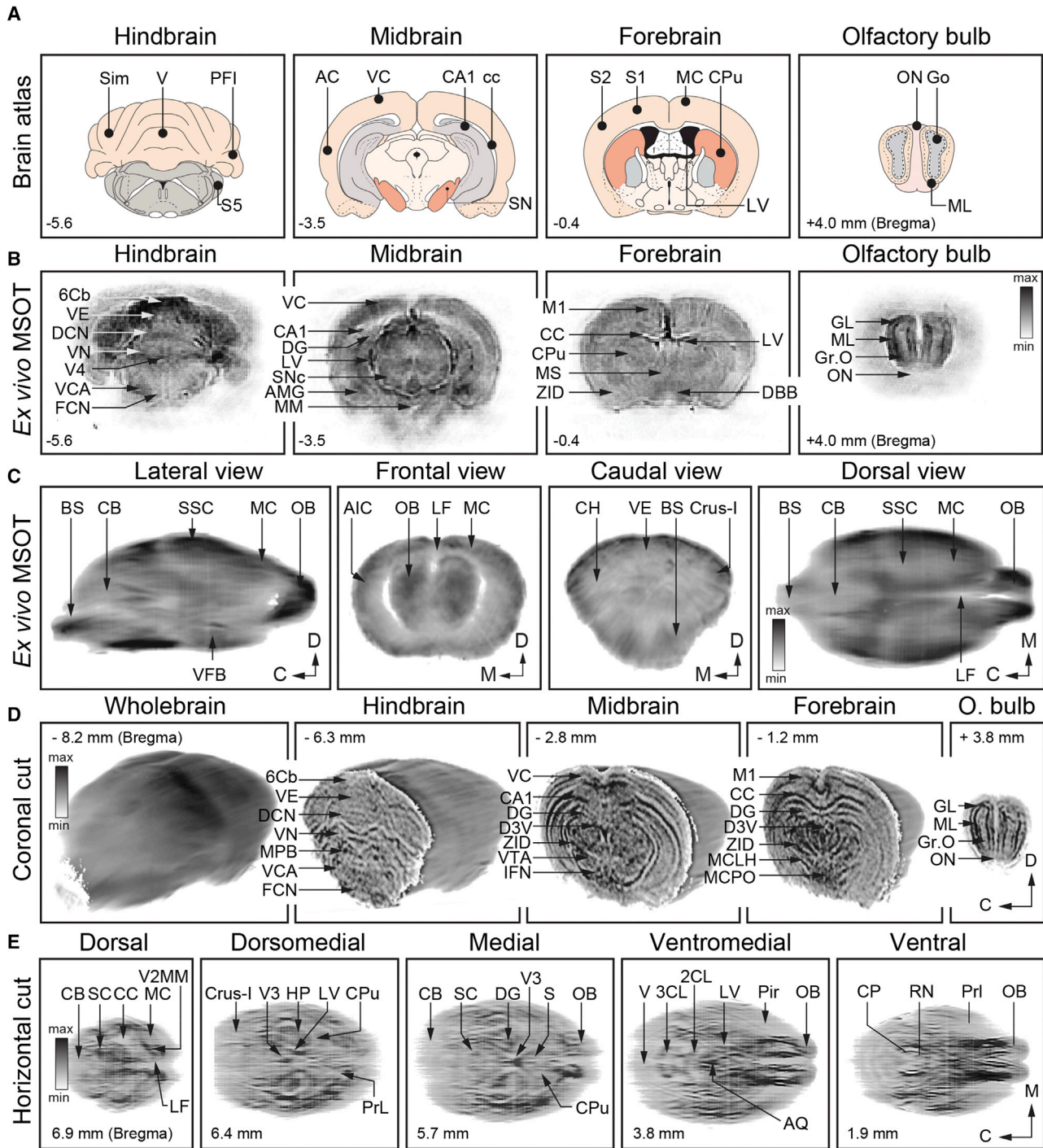


Figure 4. Structural Brain Imaging with MSOT Ex Vivo

(A and B) Schematized anatomy of a mouse brain at four different coronal planes (Bregma coordinates underneath) (A) with corresponding MSOT cross-sections of non-perfused *ex vivo* brain (B). Note exquisite structural details revealed at all planes and depths throughout entire brain cross-sections. ON, olfactory nerve; Go, granule cells of olfactory bulb; ML, mitral cell layer; S1 and S2, somatosensory cortex 1 and 2; MC, motor cortex; CPu, caudate putamen; LV, lateral ventricle; AC and VC, auditory and visual cortices; CA1, hippocampal CA1 area; cc, corpus callosum; SN, substantia nigra; Sim, simple lobule; V, vermis; PFI, paraflocculus; S5, trigeminal nucleus; Gr.O, granule cells of olfactory bulb; GL, granule cell layer; MS, medial septum; DBB, diagonal band Broca; DG, dentate gyrus; LV, lateral ventricle; SNc, substantia nigra pars compacta; AMG, amygdala; MM, medial mammillary nucleus; 6Cb, cerebellar lobule 6; VE, vermis; DCN, deep cerebellar nucleus; VN, vestibular nucleus; V4, fourth ventricle; VCN, ventral cochlear nucleus; FNC, facial nucleus.

(legend continued on next page)

advances in neuroimaging, there is pressing need for technologies and methods enabling noninvasive scalable observations of static and dynamic processes in the brain. This is particularly pertinent to small-animal neuroimaging applications, where miniature scales and weak signals impose major challenges. As a highly promising interrogation method, optoacoustic imaging has shown great potential for a range of applications in murine neuroimaging. However, up until now, all of the major assets of optoacoustic imaging have been underrated or overlooked (Ovsepian et al., 2017). Much emphasis has been placed on resolving the vasculature on the brain surface and analysis of the neurovascular response in the cortex using an open-skull approach (Liao et al., 2012; Nasirivanaki et al., 2014; Tang et al., 2015; Wang et al., 2003, 2013; Yao et al., 2015), with little progress made on systematic studies of processes and functions unfolding in the deeper compartments within the intact brain. Recently, an attempt has been made to visualize the functional connectome across an entire brain cross-section in craniotomized rats; however, images were acquired showing grossly distorted vascularization, possibly due to data overprocessing (Li et al., 2017).

In this study, we applied MSOT for high-resolution mapping of large-scale neurovascular dynamics in cross-sections of the mouse brain in response to somatosensory whisker inputs. We visualized and spectrally decomposed hemodynamic changes related to processing and allocation of whisker signals along the entire subcortical-cortical axis of the forebrain, to map Hb and HbO₂ gradients and tissue oxygenation level changes in multiple anatomical planes and brain compartments. Using the same modality, we also obtained scans of mouse brains with significant structural detail, based on intrinsic chromophores and exogenous contrast agents. These unveiled a close-to-perfect match between key anatomical features as revealed by MSOT with those discovered using customary histology and microscopy. The strong central representation along with the well-defined connectivity and discreet response to whisker inputs (Brecht and Sakmann, 2002; Feldmeyer et al., 2013; Petersen, 2007) render the whisker somatosensory system an ideal experimental model, enabling access to fundamental neurobiological processes using neuroimaging and electrophysiological methods (Berger et al., 2007; Grinvald et al., 1986; Petersen et al., 2001; Yang et al., 1996). In agreement with results of optical imaging and neurophysiological reports, our MSOT scans showed strong activation of the barrel cortex by repetitive whisker inputs. The stimulation and type of anesthesia used in

this study were based on careful consideration of numerous reports that investigated functional dynamics within this sensory system (Berger et al., 2007; Jonckers et al., 2015; Petersen et al., 2003; Yang et al., 1997). Unlike focusing on cellular-resolution microscopic readouts of functional changes in small neuronal groups within the superficial cortical layers, or low-resolution surrogate blood-oxygen-level-dependent (BOLD) signal of fMRI, we mapped and spectrally decomposed the activation and processing of somatosensory inputs by the brain at high spatial and temporal resolution. Although our observations are in general agreement with results of earlier reports showing whisker-induced hemodynamic changes in the contralateral barrel field (Feldmeyer et al., 1999; Petersen, 2007; Schubert et al., 2003), we were also able to detect expanded HbO₂ and Hb alterations involving the ipsilateral barrel cortex as well as throughout thalamic nuclei, caudal basal forebrain nuclei, and other subcortical structures. These findings are in line with neuroanatomical data on ascending lemniscal projections, which relay whisker somatosensory inputs via ventral and posterior thalamic nuclei and through extra-thalamic circuits, activating a range of subcortical structures (Brecht et al., 2004; Zaborszky et al., 2015). In this context, it is important to note that the intensity and pattern of brain responses to somatosensory inputs from whiskers can be affected by multiple factors, including the type of anesthesia, stimulus intensity, and number of activated whiskers, with prolonged strong inputs capable of activating BOLD signal over wider brain areas, including the ipsilateral to the stimulation side cortical and subcortical structures, via long-range associative connections (Alonso et al., 2008; Logothetis, 2008; Mirabella et al., 2001).

Closer analysis of the initiation and spread of the hemodynamic signals showed that Hb changes in the cortex can faithfully replicate the order of processing and integration of whisker inputs given that thalamo-cortical projections target and synchronously activate the L4 neurons, with spread of the activity from therein across entire cortical columns (Bruno and Sakmann, 2006; Petersen, 2007; Yu et al., 2014). Indeed, such activation patterns caused a faster response onset and more robust Hb signal in deep cortical layers. In contrast, HbO₂ signal changes appeared more diffuse, with higher signal intensity predominantly in the superficial layers. Although we do not have a ready explanation for such dissociation between Hb and HbO₂ signals, the compensatory nature of HbO₂ response, which in the cerebral cortex is enabled largely by activation of the superficial vascular bed via penetrating arterioles feeding deeper

(C) Lateral, frontal, caudal, and dorsal views of reconstructed mouse brain, from left to right. Maximum intensity projections. C, caudal; D, dorsal; M, medial; BS, brainstem; CB, cerebellum; SSC, somatosensory cortex; MC, motor cortex; OB, olfactory bulb; AIC, agranular insular cortex; LF, longitudinal fissure; CH, cerebellar hemisphere; VE, vermis; Crus-1, cerebellar crus 1.

(D) MSOT of the whole brain and series of cross-sections at four different planes. 6Cb, sixth cerebellar lobule; VE, vermis; DCN, deep cerebellar nucleus; VN, vestibular nuclear complex; MPB, medial parabrachial nucleus; VCA, ventral cochlear nucleus; FCN, facial nucleus; VC, visual cortex; CA1, CA1 area; DG, dentate gyrus; D3V, dorsal 3 ventricle; ZID, zona incerta dorsalis; VTA, ventral tegmental area; IFN, interfacicular nucleus; M1, motor cortex; CC, corpus callosum; MCLH, magnocellular lateral hypothalamus; MCPO, magnocellular preoptic nucleus; GL, glomerular layer; ML, mitral cell layer; Gr.O, granule cell layer; ON, olfactory nerve.

(E) Horizontal MSOT sections of the mouse brain at five (D, dorsal; DM, dorso-medial; M, medial; MV, medio-ventral; and V, ventral) planes with reference to interaural plane (distance in millimeters). CB, cerebellum; SC, superior colliculus; CC, corpus callosum; MC, motor cortex; V2MM, secondary visual cortex; LF, longitudinal fissure; V3, ventricle 3; HP, hippocampus; LV, lateral ventricle; CPu, caudate putamen; PrL, pre-limbic cortex; DG, dentate gyrus; S, septum; OB, olfactory bulb; V, vermis; 3CL, 3 cerebellar lobule; 2CL, 2 cerebellar lobule; AQ, aqueduct cerebral; Pir, piriform cortex; CP, cerebellar peduncle; RN, reticular nucleus; PrL, prelimbic cortex.

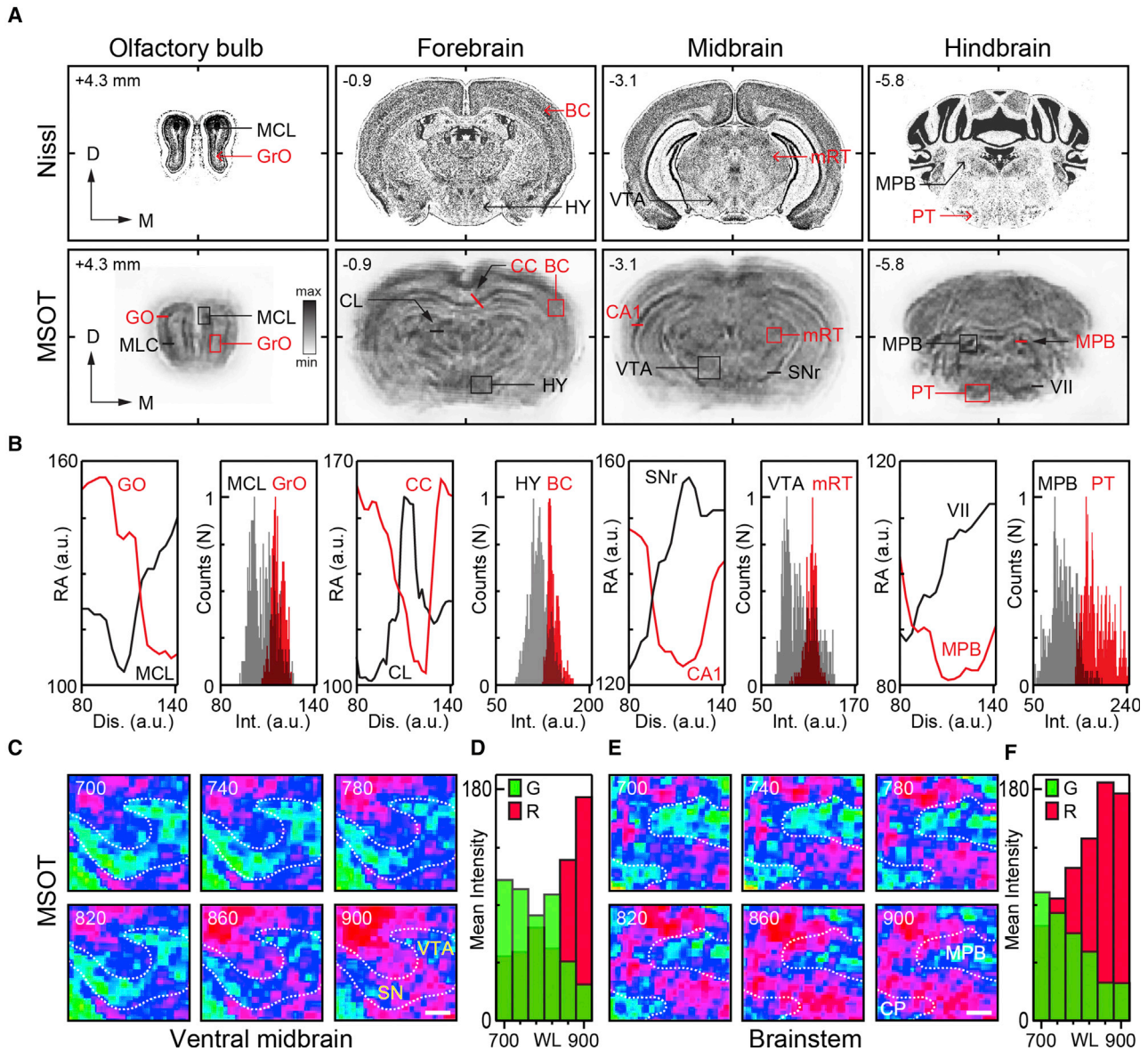


Figure 5. Morphometry and Correlation of Anatomical Features Revealed by MSOT with Those of Histochemistry

(A) Typical Nissl-stained mouse brain sections at consecutive planes (top) with corresponding MSOT images (bottom) (millimeters from bregma) (modified with permission from <http://atlas.brain-map.org/atlas>). Note close resemblance between major features of two sets of images. MCL, mitral cell layer; GrO, granule cell layer; BC, barrel cortex; HY, hypothalamus; VTA, ventral tegmental area; mRT, mesencephalic reticular thalamic nucleus; MPB, medial parabrachial nucleus; PT, pyramidal tract; CL, central thalamic nucleus; CC, corpus callosum; SN, substantia nigra; CA1, hippocampal CA1 region; VII, facial nucleus.

(B) Intensity profile graphs and absorption density distribution histograms of selected structures marked in (A) verifying the feasibility of semiquantitative morphometry using MSOT scans of *ex vivo* mouse brain.

(C and D) MSOT images of the VTA and SNc area of the midbrain taken at different wavelengths (C) with representation of spectral changes attributable to melanin-rich structures (blue) in the region (D). (C) Scale bar: 100 μ m.

(E and F) Spectral map of the MPB and cerebellar peduncle (CP) region of medulla (E) with representation of spectral changes (F) presumably due to presence of melanin in the region (between 700 and 900 nm). Scale bar: 100 μ m. Note wavelength-dependent changes in the spectral content of MSOT images over the analyzed range (ratio of red and green pixels in C and E plotted in D and F).

tissue, could account for the stronger HbO₂ signal in the superficial layers (Nishimura et al., 2007; Schaffer et al., 2006; Yu et al., 2014). We would like to stress, however, that at present the coincidence and extent of coupling between the neuronal activity and BOLD responses remain open for debate and require

further in-depth studies. Nevertheless, the specificity of activation of whisker inputs as demonstrated herein was verified by the absence of Hb and HbO₂ signals in anatomical planes lacking representations of somatosensory whisker inputs (Figures 2A–2C).

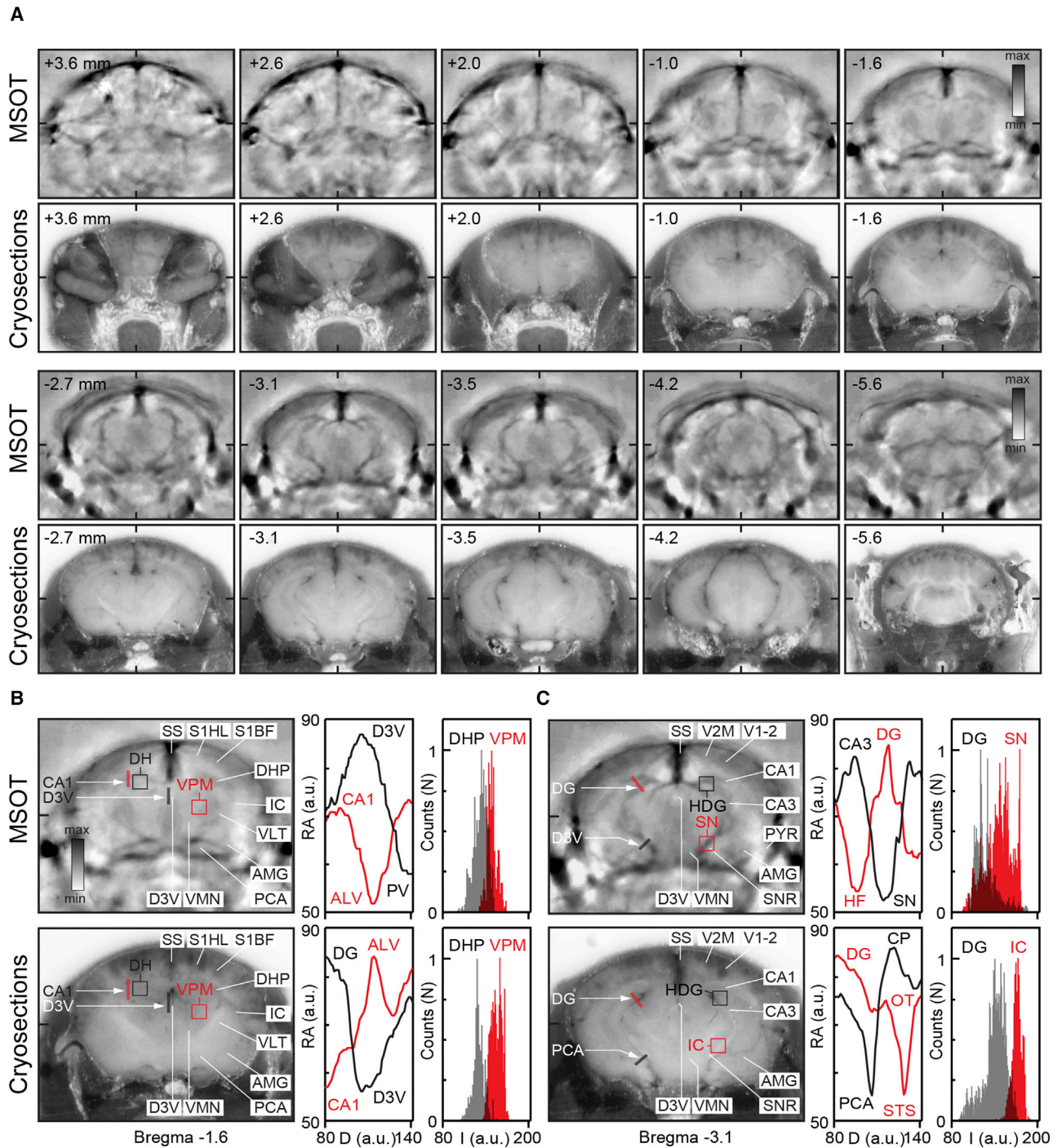


Figure 6. Label-Free Anatomical MSOT of Intact Mouse Brain *In Vivo*

(A) Series of consecutive MSOT cross-sections acquired *in vivo* (MSOT, average of 10 frames) and corresponding low-power images of the same frozen mouse brain captured on the cryo-slicer (cryosections). Note numerous exquisite structural details revealed by MSOT at all anatomical planes and depths throughout the entire brain cross-sections, with their nearly perfect correspondence with those captured using a high-resolution digital camera.

(B and C) Anatomical images and intensity profile graphs with absorption density distribution analysis of selected anatomical structures (bregma -1.6 mm, B, and bregma -3.1 mm, C) (red and black lines and boxed areas) demonstrating the utility of label-free MSOT for semiquantitative morphometry and neuroanatomical measurements *in vivo* in intact mice. SS, sagittal sinus; S1HL, somatosensory cortex hindlimb area; S1BF, somatosensory cortex barrel field; DHP, dorsal hippocampus; CA1, hippocampal CA1 area; VPM, ventral posterior-medial thalamic nucleus; IC, internal capsule; VLT, ventrolateral thalamic nucleus; VMN, ventromedial thalamic nucleus; AMG, amygdala; D3V, third ventricle; PCA, posterior central artery; PV, periventricular nucleus; ALV, stratum alveus; SN, substantia nigra; CP, cerebral peduncle; OT, optical tract; HF, hippocampal fissure; STS, sagittal transverse sinus; DG, dentate gyrus. Scale bar: $100 \mu\text{m}$.

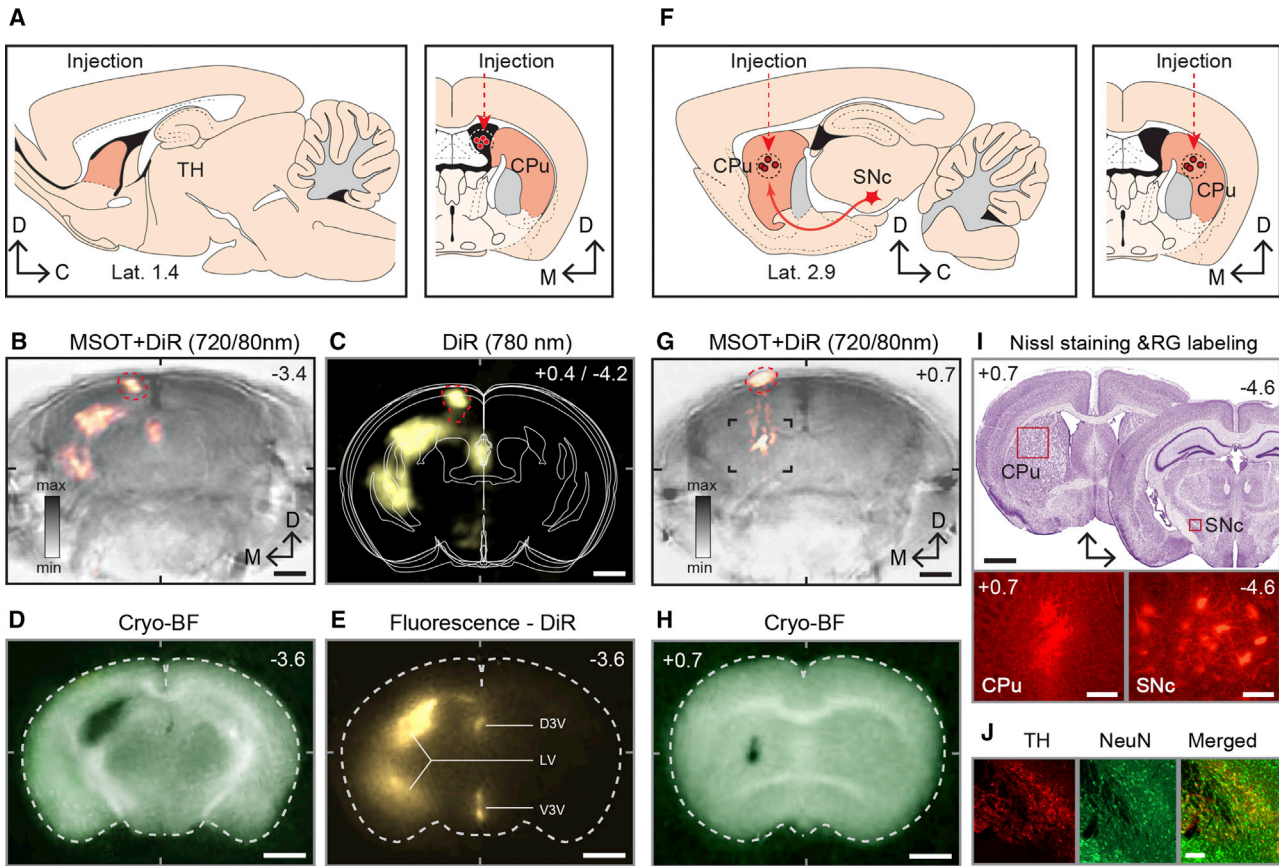


Figure 7. Enhancing Structural Brain Imaging with MSOT Using Exogenous Contrasts

(A–E) Visualizing mouse ventricular system with MSOT using NIR Di-R tracer.

(A) A schematic of the sagittal and coronal brain sections showing the site of intraventricular injection of a tracer. Anatomical references: CPu, caudate putamen; TH, thalamus.

(B and C) MSOT cross-section of the mouse brain overlaid with unmixed and reconstructed images of the cerebral ventricles (B) with corresponding simplified schematics of brain cross-sections between -2.6 and -4.0 mm of bregma (C).

(D and E) Histological verification of the Di-R injection site (D) and ventricular labeling using cryo-slicing and fluorescence light microscopy (E). Anatomical references: D3V, dorsal 3 ventricle; LV, lateral ventricle; V3V ventral 3 ventricle.

(F) A schematic of the sagittal and coronal brain sections with the site of NIR Di-R infusion revealed in dorsal striatum for retrograde labeling of SN dopaminergic projection neurons.

(G and H) Anatomical MSOT cross-section of the mouse brain overlaid with unmixed and reconstructed images of tracer injection plane (G) with histological verification (H).

(I) Validation of the injection sites and the location of SN shown in Nissl-stained brain sections and in fluorescence microscopic images of the injections site in CPu and retrogradely labeled neurons in the SNc.

(J) Immunofluorescence verification of dopaminergic neurons using anti-tyrosinase antibody and neuron-specific marker NeuN.

With respect to anatomical MSOT imaging, it is critical to note that, within the NIR range (700–900 nm), in addition to Hb, other endogenous absorbers can contribute constructively toward the formation of structural images, revealing exquisite anatomical details across entire brain cross-sections. In intact animals, as we have shown, these features are strongly masked by an overwhelming hemoglobin signal but can be partly recovered using special imaging conditions and data processing. While the contribution of individual absorbers in the formation of anatomical images remains to be characterized, water, cytochromes, lipid, and melanin are expected to play a major role (Jacques, 2013; Ovsepian et al., 2017; Weber et al., 2016; Yao and Wang, 2014). As shown, structures such as the cerebral cortex,

hippocampus, corpus callosum, basal ganglia, thalamic nuclei, ventricular system, olfactory bulb, cerebellum, together with a range of brainstem formations could be readily distinguished and quantified on MSOT scans by simple semi-quantitative analytical tools and spectral decomposition methods. It is reasonable to assume that, with its relatively uniform distribution in the brain, water absorption, like that of hemoglobin, also contributes toward the background signal, while the different density of proteins and lipids are expected to play key roles toward formation of structural features in the neuron-rich cerebral cortex and hippocampus, as well as in deep nuclei. Likewise, fat is expected to contribute and shape myelinated bundles and white-matter-rich hubs (Ovsepian et al., 2017). Clearcut appearance

of neuro-melanin-rich midbrain dopaminergic and adrenergic nuclei (Barden and Levine, 1983; Saper and Petito, 1982) as revealed with MSOT are also of considerable interest as this could potentially serve as a biomarker for studies of neurodegenerative disease affecting these major supra-spinal hubs. As shown here, anatomical MSOT neuroimaging can be further enhanced using exogenous contrast agents. However, at this point, mapping the connectome and major neural projections with tracers seems to be over-ambitious due to the inherent low sensitivity of MSOT, urging further research and optimization of hardware and experimental procedures.

In summary, our results show the powerful capabilities of MSOT for functional and structural neuroimaging, and highlight some limitations and areas for future optimization. Given additional research and refinement, MSOT is expected to advance noninvasive neuroimaging of small-animal models onto a new level, offering an impressive means for addressing a wide range of outstanding questions, with implications for basic neurobiology and translational neuroscience.

STAR★METHODS

Detailed methods are provided in the online version of this paper and include the following:

- KEY RESOURCES TABLE
- CONTACT FOR REAGENT AND RESOURCE SHARING
- EXPERIMENTAL MODEL AND SUBJECT DETAILS
- METHOD DETAILS
 - Multispectral optoacoustic tomography (MSOT)
 - Brain imaging with MSOT
 - Di-R injection into the brain and immunohistochemistry
- QUANTIFICATION AND STATISTICAL ANALYSIS

SUPPLEMENTAL INFORMATION

Supplemental Information includes six figures, one table, and six videos and can be found with this article online at <https://doi.org/10.1016/j.celrep.2019.02.020>.

ACKNOWLEDGMENTS

The research leading to these results has received funding from the Deutsche Forschungsgemeinschaft (DFG), Germany (Reinhard Koselleck award “High resolution near-field thermoacoustic sensing and imaging”, NT 3/9-1; Gottfried Wilhelm Leibniz Prize 2013, NT 3/10-1); EIT Health (FiBrUS—Mammography matters: Fighting breast cancer with workflow optimized ultrasound screening; 18202); the European Union project CosmoPHOS (FP7-NMP-2012-LARGE-6, Contract 310337); and the European Union’s Horizon 2020 research and innovation programme under grant agreement No. 761214. The materials presented and views expressed here are the responsibility of the author(s) only. The EU Commission takes no responsibility for any use made of the information set out. S.O.O. was also supported by the Project LO1611 from the MEYS under the NPU I program.

AUTHOR CONTRIBUTIONS

S.V.O. and I.O. designed the study. I.O., A.G., H.Y., J.M.-N., and S.V.O. performed the experiments. A.G. and G.S. developed the stimulation system. S.G. provided technical support. I.O., H.Y., J.M.-N., P.S., and S.V.O. conducted data analysis and interpretation. S.V.O., I.O., V.B.O., and V.N.

wrote the manuscript. All authors read and approved the final version of the manuscript.

DECLARATION OF INTERESTS

The authors declare no competing interests.

Received: April 25, 2018

Revised: January 7, 2019

Accepted: February 4, 2019

Published: March 5, 2019

REFERENCES

- Alonso, B.d.C., Lowe, A.S., Dear, J.P., Lee, K.C., Williams, S.C., and Finnerty, G.T. (2008). Sensory inputs from whisking movements modify cortical whisker maps visualized with functional magnetic resonance imaging. *Cereb. Cortex* 18, 1314–1325.
- Barden, H., and Levine, S. (1983). Histochemical observations on rodent brain melanin. *Brain Res. Bull.* 10, 847–851.
- Beard, P. (2011). Biomedical photoacoustic imaging. *Interface Focus* 1, 602–631.
- Berger, T., Borgdorff, A., Crochet, S., Neubauer, F.B., Lefort, S., Fauvet, B., Ferezou, I., Carleton, A., Lüscher, H.R., and Petersen, C.C. (2007). Combined voltage and calcium epifluorescence imaging in vitro and in vivo reveals subthreshold and suprathreshold dynamics of mouse barrel cortex. *J. Neurophysiol.* 97, 3751–3762.
- Boas, D.A., Dale, A.M., and Franceschini, M.A. (2004). Diffuse optical imaging of brain activation: approaches to optimizing image sensitivity, resolution, and accuracy. *Neuroimage* 23 (Suppl 1), S275–S288.
- Brecht, M., and Sakmann, B. (2002). Whisker maps of neuronal subclasses of the rat ventral posterior medial thalamus, identified by whole-cell voltage recording and morphological reconstruction. *J. Physiol.* 538, 495–515.
- Brecht, M., Krauss, A., Muhammad, S., Sinai-Esfahani, L., Bellanca, S., and Margrie, T.W. (2004). Organization of rat vibrissa motor cortex and adjacent areas according to cytoarchitectonics, microstimulation, and intracellular stimulation of identified cells. *J. Comp. Neurol.* 479, 360–373.
- Bruno, R.M., and Sakmann, B. (2006). Cortex is driven by weak but synchronously active thalamocortical synapses. *Science* 312, 1622–1627.
- Burton, N.C., Patel, M., Morscher, S., Driessen, W.H., Claussen, J., Beziere, N., Jetzfellner, T., Taruttis, A., Razansky, D., Bednar, B., and Ntziachristos, V. (2013). Multispectral opto-acoustic tomography (MSOT) of the brain and glioblastoma characterization. *Neuroimage* 65, 522–528.
- Chen, X., Leischner, U., Rochefort, N.L., Nelken, I., and Konnerth, A. (2011). Functional mapping of single spines in cortical neurons in vivo. *Nature* 475, 501–505.
- Culver, J.P., Durduran, T., Furuya, D., Cheung, C., Greenberg, J.H., and Yodh, A.G. (2003). Diffuse optical tomography of cerebral blood flow, oxygenation, and metabolism in rat during focal ischemia. *J. Cereb. Blood Flow Metab.* 23, 911–924.
- Dean-Ben, X.L., Ntziachristos, V., and Razansky, D. (2012). Acceleration of optoacoustic model-based reconstruction using angular image discretization. *IEEE Trans. Med. Imaging* 31, 1154–1162.
- Denic, A., Macura, S.I., Mishra, P., Gamez, J.D., Rodriguez, M., and Pirko, I. (2011). MRI in rodent models of brain disorders. *Neurotherapeutics* 8, 3–18.
- Dombeck, D.A., Harvey, C.D., Tian, L., Looger, L.L., and Tank, D.W. (2010). Functional imaging of hippocampal place cells at cellular resolution during virtual navigation. *Nat. Neurosci.* 13, 1433–1440.
- Eggebrecht, A.T., Ferradal, S.L., Robichaux-Viehoever, A., Hassanpour, M.S., Dehghani, H., Snyder, A.Z., Hershey, T., and Culver, J.P. (2014). Mapping distributed brain function and networks with diffuse optical tomography. *Nat. Photonics* 8, 448–454.

- Errico, C., Pierre, J., Pezet, S., Desailly, Y., Lenkei, Z., Couture, O., and Tanter, M. (2015). Ultrafast ultrasound localization microscopy for deep super-resolution vascular imaging. *Nature* *527*, 499–502.
- Farahani, K., Sinha, U., Sinha, S., Chiu, L.C., and Lufkin, R.B. (1990). Effect of field strength on susceptibility artifacts in magnetic resonance imaging. *Comput. Med. Imaging Graph.* *14*, 409–413.
- Feldmeyer, D., Egger, V., Lubke, J., and Sakmann, B. (1999). Reliable synaptic connections between pairs of excitatory layer 4 neurones within a single “barrel” of developing rat somatosensory cortex. *J. Physiol.* *521*, 169–190.
- Feldmeyer, D., Brecht, M., Helmchen, F., Petersen, C.C., Poulet, J.F., Staiger, J.F., Luhmann, H.J., and Schwarz, C. (2013). Barrel cortex function. *Prog. Neurobiol.* *103*, 3–27.
- Franklin, K.B.J., and Paxinos, G. (2008). *The Mouse Brain in Stereotaxic Coordinates* (Elsevier).
- Gesnik, M., Blaize, K., Deffieux, T., Gennisson, J.L., Sahel, J.A., Fink, M., Picaud, S., and Tanter, M. (2017). 3D functional ultrasound imaging of the cerebral visual system in rodents. *Neuroimage* *149*, 267–274.
- Gottschalk, S., Fehm, T.F., Deán-Ben, X.L., Tsytsarev, V., and Razansky, D. (2017). Correlation between volumetric oxygenation responses and electrophysiology identifies deep thalamocortical activity during epileptic seizures. *Neurophotonics* *4*, 011007.
- Grienberger, C., Chen, X., and Konnerth, A. (2014). NMDA receptor-dependent multidendrite Ca^{2+} spikes required for hippocampal burst firing in vivo. *Neuron* *81*, 1274–1281.
- Grinvald, A., Lieke, E., Frostig, R.D., Gilbert, C.D., and Wiesel, T.N. (1986). Functional architecture of cortex revealed by optical imaging of intrinsic signals. *Nature* *324*, 361–364.
- Helmchen, F., and Denk, W. (2005). Deep tissue two-photon microscopy. *Nat. Methods* *2*, 932–940.
- Hillman, E.M. (2007). Optical brain imaging in vivo: techniques and applications from animal to man. *J. Biomed. Opt.* *12*, 051402.
- Hong, G., Diao, S., Chang, J., Antaris, A.L., Chen, C., Zhang, B., Zhao, S., Atchinn, D.N., Huang, P.L., Andreasson, K.I., et al. (2014). Through-skull fluorescence imaging of the brain in a new near-infrared window. *Nat. Photonics* *8*, 723–730.
- Hoyer, C., Gass, N., Weber-Fahr, W., and Sartorius, A. (2014). Advantages and challenges of small animal magnetic resonance imaging as a translational tool. *Neuropsychobiology* *69*, 187–201.
- Jacques, S.L. (2013). Optical properties of biological tissues: a review. *Phys. Med. Biol.* *58*, R37–R61.
- Jonckers, E., Shah, D., Hamaide, J., Verhoye, M., and Van der Linden, A. (2015). The power of using functional fMRI on small rodents to study brain pharmacology and disease. *Front. Pharmacol.* *6*, 231.
- Kerr, J.N., and Denk, W. (2008). Imaging in vivo: watching the brain in action. *Nat. Rev. Neurosci.* *9*, 195–205.
- Laufer, J., Zhang, E., Raivich, G., and Beard, P. (2009). Three-dimensional noninvasive imaging of the vasculature in the mouse brain using a high resolution photoacoustic scanner. *Appl. Opt.* *48*, D299–D306.
- Li, L., Zhu, L., Ma, C., Lin, L., Yao, J., Wang, L., Maslov, K., Zhang, R., Chen, W., Shi, J., and Wang, L.V. (2017). Single-impulse panoramic photoacoustic computed tomography of small-animal whole-body dynamics at high spatiotemporal resolution. *Nat. Biomed. Eng.* *1*, 0071.
- Liao, L.D., Lin, C.T., Shih, Y.Y., Duong, T.Q., Lai, H.Y., Wang, P.H., Wu, R., Tsang, S., Chang, J.Y., Li, M.L., and Chen, Y.Y. (2012). Transcranial imaging of functional cerebral hemodynamic changes in single blood vessels using in vivo photoacoustic microscopy. *J. Cereb. Blood Flow Metab.* *32*, 938–951.
- Lin, L., Xia, J., Wong, T.T., Li, L., and Wang, L.V. (2015). In vivo deep brain imaging of rats using oral-cavity illuminated photoacoustic computed tomography. *J. Biomed. Opt.* *20*, 016019.
- Logothetis, N.K. (2008). What we can do and what we cannot do with fMRI. *Nature* *453*, 869–878.
- Macé, E., Montaldo, G., Cohen, I., Baulac, M., Fink, M., and Tanter, M. (2011). Functional ultrasound imaging of the brain. *Nat. Methods* *8*, 662–664.
- Mirabella, G., Battiston, S., and Diamond, M.E. (2001). Integration of multiple-whisker inputs in rat somatosensory cortex. *Cereb. Cortex* *11*, 164–170.
- Nasirivanaki, M., Xia, J., Wan, H., Bauer, A.Q., Culver, J.P., and Wang, L.V. (2014). High-resolution photoacoustic tomography of resting-state functional connectivity in the mouse brain. *Proc. Natl. Acad. Sci. USA* *111*, 21–26.
- Nishimura, N., Schaffer, C.B., Friedman, B., Lyden, P.D., and Kleinfeld, D. (2007). Penetrating arterioles are a bottleneck in the perfusion of neocortex. *Proc. Natl. Acad. Sci. USA* *104*, 365–370.
- Ntziachristos, V. (2010). Going deeper than microscopy: the optical imaging frontier in biology. *Nat. Methods* *7*, 603–614.
- Ntziachristos, V., Ripoll, J., Wang, L.V., and Weissleder, R. (2005). Looking and listening to light: the evolution of whole-body photonic imaging. *Nat. Biotechnol.* *23*, 313–320.
- Olefir, I., Mercep, E., Burton, N.C., Ovsepian, S.V., and Ntziachristos, V. (2016). Hybrid multispectral photoacoustic and ultrasound tomography for morphological and physiological brain imaging. *J. Biomed. Opt.* *21*, 86005.
- Osmanski, B.F., Pezet, S., Ricobaraza, A., Lenkei, Z., and Tanter, M. (2014). Functional ultrasound imaging of intrinsic connectivity in the living rat brain with high spatiotemporal resolution. *Nat. Commun.* *5*, 5023.
- Ouzounov, D.G., Wang, T., Wang, M., Feng, D.D., Horton, N.G., Cruz-Hernández, J.C., Cheng, Y.T., Reimer, J., Toliás, A.S., Nishimura, N., and Xu, C. (2017). In vivo three-photon imaging of activity of GCaMP6-labeled neurons deep in intact mouse brain. *Nat. Methods* *14*, 388–390.
- Ovsepian, S.V., Olefir, I., Westmeyer, G., Razansky, D., and Ntziachristos, V. (2017). Pushing the boundaries of neuroimaging with photoacoustics. *Neuron* *96*, 966–988.
- Perron, A., Mutoh, H., Launey, T., and Knöpfel, T. (2009). Red-shifted voltage-sensitive fluorescent proteins. *Chem. Biol.* *16*, 1268–1277.
- Peterka, D.S., Takahashi, H., and Yuste, R. (2011). Imaging voltage in neurons. *Neuron* *69*, 9–21.
- Petersen, C.C. (2007). The functional organization of the barrel cortex. *Neuron* *56*, 339–355.
- Petersen, R.S., Panzeri, S., and Diamond, M.E. (2001). Population coding of stimulus location in rat somatosensory cortex. *Neuron* *32*, 503–514.
- Petersen, C.C., Grinvald, A., and Sakmann, B. (2003). Spatiotemporal dynamics of sensory responses in layer 2/3 of rat barrel cortex measured in vivo by voltage-sensitive dye imaging combined with whole-cell voltage recordings and neuron reconstructions. *J. Neurosci.* *23*, 1298–1309.
- Razansky, D., Buehler, A., and Ntziachristos, V. (2011). Volumetric real-time multispectral photoacoustic tomography of biomarkers. *Nat. Protoc.* *6*, 1121–1129.
- Saper, C.B., and Petito, C.K. (1982). Correspondence of melanin-pigmented neurons in human brain with A1-A14 catecholamine cell groups. *Brain* *105*, 87–101.
- Schaffer, C.B., Friedman, B., Nishimura, N., Schroeder, L.F., Tsai, P.S., Ebner, F.F., Lyden, P.D., and Kleinfeld, D. (2006). Two-photon imaging of cortical surface microvessels reveals a robust redistribution in blood flow after vascular occlusion. *PLoS Biol.* *4*, e22.
- Schubert, D., Kötter, R., Zilles, K., Luhmann, H.J., and Staiger, J.F. (2003). Cell type-specific circuits of cortical layer IV spiny neurons. *J. Neurosci.* *23*, 2961–2970.
- Siegel, A., Marota, J.J., and Boas, D. (1999). Design and evaluation of a continuous-wave diffuse optical tomography system. *Opt. Express* *4*, 287–298.
- Stein, E.W., Maslov, K., and Wang, L.V. (2009). Noninvasive, in vivo imaging of blood-oxygenation dynamics within the mouse brain using photoacoustic microscopy. *J. Biomed. Opt.* *14*, 020502.
- Stettler, D.D., Yamahachi, H., Li, W., Denk, W., and Gilbert, C.D. (2006). Axons and synaptic boutons are highly dynamic in adult visual cortex. *Neuron* *49*, 877–887.

- Tang, J., Xi, L., Zhou, J., Huang, H., Zhang, T., Carney, P.R., and Jiang, H. (2015). Noninvasive high-speed photoacoustic tomography of cerebral hemodynamics in awake-moving rats. *J. Cereb. Blood Flow Metab.* *35*, 1224–1232.
- Taruttis, A., and Ntziachristos, V. (2015). Advances in real-time multispectral optoacoustic imaging and its applications. *Nat. Photonics* *9*, 219–227.
- Tiran, E., Ferrier, J., Deffieux, T., Gennisson, J.L., Pezet, S., Lenkei, Z., and Tanter, M. (2017). Transcranial functional ultrasound imaging in freely moving awake mice and anesthetized young rats without contrast agent. *Ultrasound Med. Biol.* *43*, 1679–1689.
- Tzoumas, S., Kravtsov, A., Gao, Y., Buehler, A., and Ntziachristos, V. (2016). Statistical molecular target detection framework for multispectral optoacoustic tomography. *IEEE Trans. Med. Imaging* *35*, 2534–2545.
- Wang, X., Pang, Y., Ku, G., Xie, X., Stoica, G., and Wang, L.V. (2003). Noninvasive laser-induced photoacoustic tomography for structural and functional in vivo imaging of the brain. *Nat. Biotechnol.* *21*, 803–806.
- Wang, L., Maslov, K., and Wang, L.V. (2013). Single-cell label-free photoacoustic flowography in vivo. *Proc. Natl. Acad. Sci. USA* *110*, 5759–5764.
- Weber, J., Beard, P.C., and Bohndiek, S.E. (2016). Contrast agents for molecular photoacoustic imaging. *Nat. Methods* *13*, 639–650.
- Willem, M., Tahirovic, S., Busche, M.A., Ovsepian, S.V., Chafai, M., Kootar, S., Hornburg, D., Evans, L.D., Moore, S., Daria, A., et al. (2015). η -Secretase processing of APP inhibits neuronal activity in the hippocampus. *Nature* *526*, 443–447.
- Wilt, B.A., Burns, L.D., Wei Ho, E.T., Ghosh, K.K., Mukamel, E.A., and Schnitzer, M.J. (2009). Advances in light microscopy for neuroscience. *Annu. Rev. Neurosci.* *32*, 435–506.
- Yang, Q.X., Smith, M.B., and Wang, J. (2006). Magnetic Susceptibility Effects in High Field MRI. *Vol. 26* (Springer).
- Yang, X., Hyder, F., and Shulman, R.G. (1996). Activation of single whisker barrel in rat brain localized by functional magnetic resonance imaging. *Proc. Natl. Acad. Sci. USA* *93*, 475–478.
- Yang, X., Hyder, F., and Shulman, R.G. (1997). Functional MRI BOLD signal coincides with electrical activity in the rat whisker barrels. *Magn. Reson. Med.* *38*, 874–877.
- Yao, J., and Wang, L.V. (2014). Photoacoustic brain imaging: from microscopic to macroscopic scales. *Neurophotonics* *1*, 011003.
- Yao, J., Wang, L., Yang, J.M., Maslov, K.I., Wong, T.T., Li, L., Huang, C.H., Zou, J., and Wang, L.V. (2015). High-speed label-free functional photoacoustic microscopy of mouse brain in action. *Nat. Methods* *12*, 407–410.
- Yu, X., Qian, C., Chen, D.Y., Dodd, S.J., and Koretsky, A.P. (2014). Deciphering laminar-specific neural inputs with line-scanning fMRI. *Nat. Methods* *11*, 55–58.
- Zaborszky, L., Csordas, A., Mosca, K., Kim, J., Gielow, M.R., Vadasz, C., and Nadasdy, Z. (2015). Neurons in the basal forebrain project to the cortex in a complex topographic organization that reflects corticocortical connectivity patterns: an experimental study based on retrograde tracing and 3D reconstruction. *Cereb. Cortex* *25*, 118–137.

STAR★METHODS

KEY RESOURCES TABLE

REAGENT or RESOURCE	SOURCE	IDENTIFIER
Antibodies		
Chicken, polyclonal anti-TH	Abcam	CN76422
Rabbit, polyclonal anti-NeuN	Abcam	CN104225
AlexaFluor594, goat anti-chicken TH	Abcam	N150176
AlexaFluor488 goat anti-rabbit NeuN	Life Technologies	A-11008
Experimental Models: Organisms/Strains		
Nude-FOXN1 Nu/Nu mice	Jackson Laboratories	000819-B6.Cg-Foxn1 < nu > J
CD1 mice	Charles River	CrI:CD1(ICR)-022
Software and Algorithms		
IgorPro	Wavemet, Oregon	Version 6.1
A model-based reconstruction algorithm	IBMI GmbH	Dean-Ben et al., 2012
Other		
NIR Di-R	Thermo-Fisher, DE	D12731
MSOT256-TF	iThera Med. GmbH	256-TF
Nd-YAG laser pumped OPO	InnoLas Las. GmbH	Model SL450

CONTACT FOR REAGENT AND RESOURCE SHARING

Further information and requests for resources and reagents should be directed to and will be provided by the Lead Contact, Vasilis Ntziachristos (v.ntziachristos@helmholtz-muenchen.de).

EXPERIMENTAL MODEL AND SUBJECT DETAILS

Young adult Hsd:Athymic Nude-FOXN1 Nu/Nu and CD1 mice used in all experiments described in the study (Table S1) were housed in a special housing facility at 21°C and 36% ± 2% humidity. The light-dark cycles were maintained at 12 h, with food and water provided *ad libitum*. All experiments involving living animals were conducted in accordance with the institutional guidelines and procedures approved by the government of Upper Bavaria, in compliance with German Federal and European Union law. Necessary steps have been taken to reduce animal use and suffering.

METHOD DETAILS

Multispectral optoacoustic tomography (MSOT)

The MSOT (MSOT256-TF, iThera Medical GmbH, Munich, Germany) used for all imaging experiments has a cylindrically curved detector array ($R = 40$ mm), providing 270° angular coverage of the imaging specimen (Olefir et al., 2016). Figure S1A shows a schematic representation of MSOT. The detector containing 256 elements manufactured from a piezo-composite material covers up to 7.5 MHz, with 5 MHz ± 10% (−6 dB) center frequency. All channels are digitized in parallel at 10 Hz repetition and sampling rate of 40 MHz, using a custom designed data acquisition (DAQ) card. Illumination within the near infra-red (NIR, 680–940 nm) is provided by a tunable Nd-YAG laser pumped optical parametric oscillator (OPO, InnoLas Laser GmbH, Krailling, Germany) with 9 ns pulse duration, 90 mJ peak pulse energy at 750 nm wavelength with a repetition rate of 10 Hz. The laser beam multiplexed to five fiber bundles is arranged over the detector array to provide circular illumination of the imaging plane, which is fixed or moved stepwise in a rostrocaudal direction with 0.1 mm increment.

Brain imaging with MSOT

Male mice (4–8 weeks old) were used for all experiments, which were conducted under general isoflurane anesthesia. To avoid direct contact with the US coupling water medium in the imaging chamber, animals were wrapped in optically and acoustically transparent foil prior to their placement in the holder in a supine position relative to the MSOT detector array. After *in vivo* imaging sessions, mice were injected with a lethal dose of ketamine (180 mg/kg) and processed for *ex vivo* brain imaging experiments, cryo-slicing and

immunohistochemistry. For *ex vivo* MSOT, brains were excised without or after perfusion (4% PFA in 0.1 M PBS) followed by 24 h post-fixation in 4% PFA. Wavelength selection was based on experimental requirements as well as consideration of light fluence maps, and absorption spectra of endogenous chromophores of the brain (Figures S1B–S1D).

For all functional brain imaging studies, mice were anesthetized, with customized magnetic beads attached to 6–10 large whiskers of rows B, C and D of the left side, which was used as the actuator of whisker stimulation. Anesthetized mice (1.2–1.8% vaporized isoflurane in air at 0.8 L/min) were placed in the MSOT, with the level of isoflurane subsequently reduced (0.7–1.0%) to achieve stable and shallow breathing, predictive of a highly responsive brain state. A custom-made rostral mask was utilized to ensure sufficient space for free whisker movement upon application of the magnetic force, while seamless contact was maintained between the mouse head and the coupling water medium (Figure S2A; Videos S1–S3). An 'in-house' designed electromagnetic unit containing an induction coil with a metallic rod in the middle was placed in the imaging chamber in close proximity to the mouse rostrum, to generate sufficient magnetic force for whisker deflections. The latter was controlled by a customized AC amplifier and an impulse generator unit (Figure S2B) to deliver rectangular current pulses (100 ms) at 3–5 Hz frequency.

The selection of imaging planes was based on the coordinates described in the mouse brain atlas (Franklin and Paxinos, 2008), as well as on anatomical references visualized by the MSOT *in vivo*, to ensure that selected cross-sections contain the somatosensory cortex barrel field and connected thalamic nuclei. As an additional reference, we used *in vivo* MSOT brain images co-registered with *ex vivo* scans, with the latter highlighting exquisite structural details. A series of functional images from adjacent planes (1.5 mm rostral or caudal from the central plane) were also acquired to ensure brain structures displaying the most pronounced signals had been captured in MSOT studies. To safeguard fast acquisition of multispectral data, measurements of stimulation induced activities were conducted at three wavelengths: 700 nm, 800 nm, 900 nm, which correspond to the absorption optima of deoxy- and oxy-Hb (Hb = 700 nm and HbO₂ = 900 nm) and isosbestic point, a measure of the total blood volume (805 nm) (Figures S1D, S3A, and S3B). For both, structural and functional imaging studies, raw data were collected without averaging at ~3.3 Hz per each wavelength. Based on selected wavelengths, changes in Hb gradients and blood volume could be tracked over time and projected on anatomical MSOT cross-sections. After 60 s baseline imaging, whisker were stimulated over 10–30 s without interruption of the data collection, which was followed by 60 s post-stimulation recordings. For control experiments, the same protocols were followed with whiskers being not decorated with magnetic beads.

For *ex vivo* structural MSOT studies, non-perfused or perfused brains fixed with PFA were attached to a custom-made transparent rod placed in the center of the MSOT detector array, and imaged within 680–940 nm range, with 100 nm increment and 200 μm step-wise movements of the sample in the rostrocaudal direction. For *in vivo* structural MSOT, experimental procedures were similar to that of functional imaging studies except measurements were acquired along the entire rostro-caudal axis of the brain at 200 μm steps. Throughout these experiments, mice were supplied with air or transiently (30–45 s) challenged with 10% CO₂, to achieve a better contrast and visibility of deep structures. All structural imaging experiments were followed by euthanizing the mice with ketamine overdose (180 mg/kg), deep freezing and slicing (100 μm) of mice brains for correlative imaging using a Leica Cryostat CM1950.

Di-R injection into the brain and immunohistochemistry

Under deep anesthesia (ketamine 80 mg/kg and xylazine 10 mg/kg) the head of the mouse was fixed in a stereotactic frame with the skull surgically opened under local anesthesia (bupivacaine, 0.5%). Using a dental drill, small holes were bored over the dorsal cistern of the lateral ventricle (−0.34 mm bregma, 1.4 mm lateral, 1.5 mm deep) or over the caudate nucleus (+0.5 mm bregma, 1.5 mm lateral, 2.7 mm deep) (Franklin and Paxinos, 2008). NIR Di-R (Thermo-Fisher, Germany) was slowly pressure-injected (1.0 μL over 5–6 min) into the lateral ventricle or the dorsal striatum with a Hamilton syringe (22-gauge needle) followed by careful removal of the injector and wound stitching. In control experiments, similar procedures were followed except mice were injected with an equivalent volume of DMSO only. After surgery, animals were placed back into their home cage. Following 4 days recovery period, animals were used for *in vivo* and *ex vivo* MSOT brain imaging at peak Di-R absorption wavelength (Figure S1D) followed by histology and immunostaining. For the latter, coronal PFA fixed sections containing the substantia nigra were dried on a heating plate and treated with 4% PFA for 7 min, followed by rinsing with TBST (0.1 mM). The slices were blocked with 10% goat serum in TBS and Triton (0.1 mM and 0.3%, respectively) for 1 hour at room temperature. After washes of blocking solution, tissue was incubated with primary antibodies (chicken, polyclonal anti-tyrosine hydroxylase, 1:50 and rabbit, polyclonal anti-NeuN, 1:50) (Abcam, CN76422, and CN104225, respectively) diluted in TBS-Triton 0.3% in a moisture chamber at 4°C overnight. On the following day the secondary antibodies (AlexaFluor594, goat anti-chicken 1:200 for tyrosine hydroxylase and AlexaFluor488 goat anti-rabbit 1:200 for NeuN) (Abcam N150176 and Life Technologies A-11008) were added for 1 h in a moisture chamber at room temperature before and after rinsing with TBS-Triton 0.3% for 3 times over 10 min. Tissue sections were subsequently mounted with Prolong Gold anti-fade mounting media containing DAPI and viewed in a Zeiss Axio-Imager M2 Microscope. For negative control sections, all procedures were kept the same except that goat serum in TBS was used instead of primary antibodies. For *ex vivo* validation of the injection site and structural MSOT results, we performed immunohistochemistry on 10 μm thick frozen sections cut by the Leica Cryostat CM1950.

QUANTIFICATION AND STATISTICAL ANALYSIS

MSOT images were generated using a model-based reconstruction algorithm (Dean-Ben et al., 2012) with Tikhonov regularization. All acquired frames were co-registered to suppress the motion artifacts with rigid registration of the algorithm based on mutual

information, which was supplied in MATLAB. Every frame was filtered using a Gaussian filter, with standard deviation (SD) of 2 pixels (200 μm). Similar to functional MRI data (Jonckers et al., 2015), in the resulting time-series, every pixel in the frame has an associated time trace representing the change of image intensity at the corresponding location. As functional imaging studies were performed at 3 wavelengths, all acquired data consisted of 3 time series. For every pixel, the corresponding intensity and time profile were filtered in the Fourier domain, with a low-pass filter in the range of up to 0.1 Hz, to remove high-frequency noise and any irrelevant signal fluctuations. A time trace of a hemodynamic response was generated based on the canonical Hemodynamic Response Function (HRF) $hrf(t)$ convolved with a ramp function $r(t)$ representing the stimulation pattern ($r(t) = 1$ if the stimulation is on at time t and 0 otherwise), resulting in the expected response function, $f(t): f(t) = hrf(t) * r(t)$.

For temporal coherence analysis and determining the extent of the correlation of the activity between various brain subfields, intensity traces were correlated with $f(t)$. The absolute correlation values obtained for each pixel were plotted to generate a spatial correlation map. The correlation map threshold was tuned to discard pixels that do not correlate with the expected response strongly (correlation value below 0.5) or significantly ($p \leq \frac{0.05}{N}$, where N is the total number of traces considered for a specific wavelength). For every pixel p_i , the corresponding baseline intensity variability range was computed as $\mu_i \pm 2\sigma_i$, where μ_i and σ_i are the mean and standard deviation of the pixel intensity during the baseline measurement. For illustration purposes of brain activation, thresholded pixels altered by activation were overlaid in color over the anatomical images. A pixel p_i shown as active at time t has a corresponding correlation value higher than 0.5 and the corresponding intensity value at time t exceeding the baseline variability range. Pixel color is coded to represent the deviation of its value from μ_i . Pixels with the corresponding time traces having negative values were discarded as such values have no physical meaning. This, however, did not mean that the corresponding time trace did not bear information on activation. For every obtained multispectral frame, $s\text{O}_2$ was computed using a linear unmixing algorithm. To achieve better accuracy of $s\text{O}_2$ estimation, all frames were calibrated for 4 cm water absorption prior to spectral decomposition. For illustration purposes of thresholded pixels, the corresponding computed $s\text{O}_2$ values were overlaid in color on anatomical images, with pixels labeled as activated at either 700 nm or 900 nm illumination wavelengths.

For brain circuit analysis, 17 regions of interest (ROIs) were identified in MSOT brain cross-sections. Time traces corresponding to pixels in a particular region were averaged to improve the SNR. The resulting time series p_i , $i = 1 \dots 17$ were compared pairwise. Correlation values as well as the corresponding P values were computed and presented. Furthermore, for each of the investigated time series, the activation amplitude A was computed as $A = \max|p_i - \mu_i|$, where μ_i is the mean value of p_i during the baseline measurement. For seed-based correlation analysis, several seed regions have been identified. For every region, the corresponding traces have been averaged and the resulting time series was correlated to every trace outside of the seed region. The resulting correlation maps were thresholded as described above.

Anatomical MSOT images were generated through averaging 10 frames of the same anatomical planes acquired at a single specified excitation wavelength. For assessment and presentation of the Di-R data, reconstructed MSOT images were analyzed with a QL-shrinkage detection algorithm (Tzoumas et al., 2016) that estimates the spatial distribution of a contrast agent in the recorded multispectral dataset based on absorption spectrum.

In whole brain imaging studies with tracer injection, the resulting images and spatial distribution of Di-R were rendered in 3D and overlaid with anatomical images using Amira (ThermoFisher). All color maps are generated with MATLAB, while IgorPro was used for plotting graphs. Final figures were prepared using IgorPro (6.1, Wavemetrics, Oregon) and Adobe Illustrator (CS6 package). Where applicable, the mean values and standard error of the means (SEM) have been presented in graphs, to illustrate the distribution of the parameters of interest. Unpaired and paired Students t tests and one-way analysis of variance (ANOVA) have been used for variance analysis and comparison, with p values less than 0.05 defining differences as statistically significant.